Measurements of Surface River Doppler Velocities with Along-Track InSAR Using a Single Antenna

Filippo Biondi, *Member, IEEE*, Pia Addabbo, *Senior Member, IEEE*,
Carmine Clemente, *Senior Member, IEEE*, and Danilo Orlando, *Senior Member, IEEE*,

***Abstract*—Nowadays, a worldwide database containing the historical and reliable data concerning the water surface speed of rivers in not available and would be highly desirable. In order to meet this requirement, the present work is aimed at the design of an estimation procedure for water flow velocity by means of synthetic aperture radar (SAR) data. The main technical aspect of the proposed procedure is that an along-track geometry is synthesized using a single antenna and a single image. This is achieved by exploiting a multi-chromatic analysis in the Doppler domain. The application of this approach allows us to obtain Along-Track Interferometry equivalent virtual baselines much lower than the equivalent baseline corresponding to the decorrelation time of raw data preserving data coherence. The performance analysis, conducted on live airborne full-polarimetric SAR data, highlights the effectiveness of the proposed approach in providing reliable river surface velocity estimates without the need of multiple passes on the observed scene.**

***Index Terms*—Synthetic Aperture Radar, Along-track Interferometry, Doppler Sub-apertures, Multi-Chromatic Analysis, Radar, River Surface Doppler Velocity Estimation.**

I. Introduction

ALONG-track interferometry (ATI) is a synthetic aperture radar (SAR) technique which allows for the combination of two or more SAR images of the same scene. Data are acquired from different positions separated by a physical baseline along the azimuth direction. Then, the phase differences are estimated from all coregistered pixels, which are proportional to the Doppler shifts of the backscattered radar echoes. This feature can be suitably exploited to estimate the surface velocity of water masses. In this context, the classical dual-sensor ATI geometric configuration has been firstly proposed in [1] where the authors describe a new method to measure sea surface currents. The experimental results refer to an airborne implementation of the technique, tested over the San Francisco Bay near the time of maximum tidal flow and leading to a map of the east-west component of the water current. This study also underlines that only the line-of-sight (LOS) component of the targets velocities is measured by ATI. In [2], the authors investigated for the first time the application of ATI for the estimation of the ocean currents. Data have been acquired by the shuttle radar topography mission (SRTM), which used an auxiliary antenna yielding a baseline aligned with the azimuth direction of 7 m. The authors of [3] successfully obtained airborne ATI SAR data (from a sensor called RAMSES) related to the Rhone river in France. Precise LOS velocity estimates of the river surface water have been obtained. In [4], L- and C-band ATI-SAR measurements acquired over the Ulsan coast in the southeastern part of the Korean peninsula were used in order to retrieve the ocean surface current vector field. The results have been compared with a set of in-situ measurements of the water current. Three classes of estimators were proposed in [5] which exploited multi-baseline ATI acquisition and Doppler resolution for robust data inversion under different degrees of a priori information concerning the wind direction and the value of the characteristic Bragg frequency. Performance analysis and comparison with conventional ATI showed that the proposed estimators produced the accurate velocity estimates in the absence of detailed ancillary data. In [6], an analysis of the gradient-induced distortions in the surface current estimates generated by ATI-SAR systems using an airborne sensor was provided. Such a distortion was incorporated into a dual-beam ATI-SAR system designed to estimate the surface current vector using only a single aircraft pass. A pair of interferometer SAR beams squinted fore and aft with respect to the platform, respectively, were employed in [7]. Specifically, the analysis has pointed out that the azimuthal displacements of the interferometric phases were identical to those of conventional SAR and that such displacements biased the estimated surface velocity. Authors of [8] performed simultaneous measurements of the terrain heights and currents using an airborne interferometric SAR (InSAR). For the first time, a hybrid two-antenna InSAR system with both along- and across-track baseline components was used to measure high-resolution digital elevation maps (DEMs) and current fields in the Wadden sea area. Finally, in [9], [10], [11], the Doppler sub-aperture analysis was used to extrapolate coherent targets (sparse components) from the low-rank background enhancing the detection probability of small targets.

The velocity of a river's water-flow depends mainly upon the slope and the roughness of its channel. A steeper slope causes higher flow velocity, but a rougher channel decreases it. The slope of a river corresponds approximately to the topographic slope of the country it crosses. Near to the source of the river, frequently on hilly regions, the topographic slope is

Carmine Clemente's work was supported by the Engineering and Physical Sciences Research Council (EPSRC) Grant number EP/K014307/1 and the MOD University Defence Research Collaboration in Signal Processing.

Filippo Biondi is with Italian Ministry of Defence. E-mail: biopippo@gmail.com.

Pia Addabbo is with Università degli studi Giustino Fortunato, Benevento, Italy. E-mail: p.addabbo@unifortunato.eu.

Carmine Clemente is with the University of Strathclyde, Department of Electronic and Electrical Engineering, 204 George Street, G1 1XW, Glasgow, Scotland.

D. Orlando is with Università degli Studi "Niccolò Cusano," 00166 Roma, Italy. E-mail: danilo.orlando@unicusano.it.

usually very steep and going far away it gradually flattens out. In most cases, occasional irregularities in elevation occur until the last part of the river course where it becomes quite mild. Accordingly, large streams usually begin like torrents characterized to have highly turbulent flows before becoming gently flowing rivers. Authors of [12] used the mass balance data from Asian rivers together with a first-order diffusive simplification of the St. Venant-Exner equations to characterize river floodplain processes and discuss the reaction of a large model-river to a hillslope supply of eroded masses. The simple analytical solution derived for the long-term profile of the river bed shows that the system converges towards a state in which it reacts to perturbations in the erosion of the landscape by small-amplitude oscillations around an average stationary state. However, the results are based on one study case in which several regions of interests (ROIs) consists of a series of SAR patches representing some rivers which are observed from an airborne SAR sensor (UAVSAR) which characteristics are reported in [13]. Finally, other interesting works related to the application of ATI and, generally speaking, of InSAR for the estimation of heights/velocities of components belonging to moving objects in the observed scene as rivers, vegetation, maritime targets or infrastructures can be found in [14]–[31].

In this paper, a novel procedure based on azimuth multi chromatic analysis (MCA) and ATI is devised to estimate rivers surface water-flow velocities exploiting only one SAR image. More precisely, raw data are firstly filtered in the Doppler domain in order to create two sub-apertures which are, then, refocused obtaining a couple of single look complex (SLC) SAR images. It follows that azimuth resolution band of the two SLC images is half of the original resolution. The two SLC SAR images are used to form an interferogram and the phase interference is evaluated to investigate the Doppler behavior exhibited by fixed targets with respect to others sharing the same motion characteristics. The advantages of the proposed technique over classical ATI consist in the use of only one SAR image and one sensor to collect data while providing comparable performance. As a matter of fact, in this case, the ATI geometry is built-up virtually by splitting the Doppler spectrum. As a consequence, the virtual baseline is very short preserving a level of correlation which allows for interferometry as corroborated by the experimental results. Precisely, we found that the virtual baseline synthesized by the proposed method (0.24 m) is much lower than the equivalent baseline that corresponds to the decorrelation time of raw data (about 8 m).

The performance assessment is conducted on both simulated and real-recorded data. The latter have been acquired by a UAVSAR system. In a nutshell, the proposed method is capable of tracking river flow speed variations along the river itinerary. More importantly, the obtained estimates are coherent with the height measurements from a ground station confirming the effectiveness of the proposed method.

The remainder of this paper is organized as follows. The details of the estimation procedure are described in Section II. Section III contains the illustrative examples based upon both simulated and real data, while subsection III-B2 compares the estimates obtained on real data with the ground-truth. The last section concludes the paper and introduces future research in the area.

II. Estimation Procedure

In this section, the proposed estimation procedure is described in depth. However, it is important to recall that an estimate of the Doppler shift characterizing the backscattered signal can be obtained through spatial diversity. Specifically, it can be obtained by installing two antennas separated by the corresponding spatial baseline oriented along the flight direction. As a matter of fact, the phase differences between all range-azimuth resolution cells composing the two obtained images are proportional to the Doppler shifts. Such a technique is known as ATI and is different from cross-track interferometry used for topographic reconstruction. An estimate of the LOS velocity of targets can be obtained by estimating the interferogram between the master and the slave Doppler sub-apertures and the estimation procedure relies on the fact that the phase difference is proportional to the ATI spatial baseline:

$$\Delta\phi = \frac{4\pi u B}{\lambda v}, \tag{1}$$

where λ is the operating wavelength, B is the along-track spatial baseline, v is the radar velocity, and u is the LOS speed component of the targets.

In this paper, for the first time (at least to the best of authors' knowledge) the spatial diversity for velocity estimation is emulated by using a single antenna as well as a single SAR image and applying the Multi-Chromatic Analysis (MCA) along the azimuth direction. The ATI geometry is virtually synthesized by creating two sub-apertures in the frequency domain by filtering the original SAR image. This pair of new images emulates a virtual baseline which is then used to perform the ATI. Such an approach represents the main contribution of this work. In order to clarify the proposed approach, we observe that a real SAR antenna with a physical along-track aperture L (see Figure 1 (a)), exhibits a beam-width equal to:

$$\phi_D = \frac{\lambda}{L}, \tag{2}$$

while the frequency bandwidth associated with the Doppler shifts within this beam-width is given by:

$$\Delta f_D \approx \frac{2v\phi_D}{\lambda} = 2\frac{v}{L}, \tag{3}$$

where v is the platform velocity. The trend of Doppler frequency with respect to a stationary target as a function of the sensor acquisition time is represented in Figure 1 (b). This point target, when approached by the antenna's radiation footprint, has a maximum Doppler value. This Doppler is decreasing more and more and, passing through the Doppler centroid, it reaches the minimum Doppler value when exiting from the radiation footprint. Figure 1 (c) represents the response versus time of the adapted filter that is a response opposite to that of the target. Now, equation (3) can be exploited in what follows to "synthesize" a virtual physical baseline between two aforementioned Doppler sub-apertures.

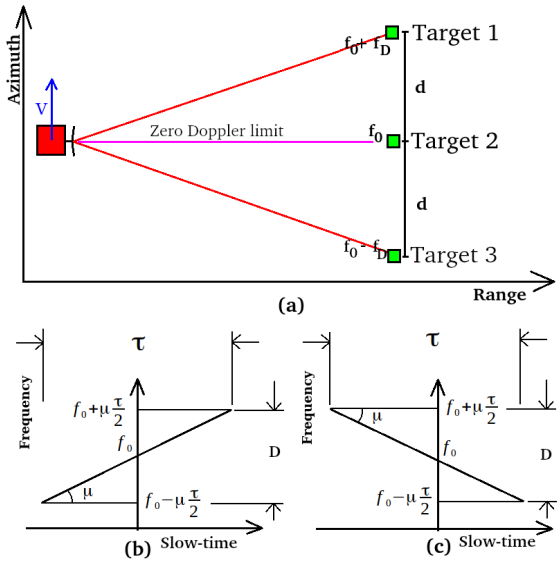

Fig. 1. SAR geometry.

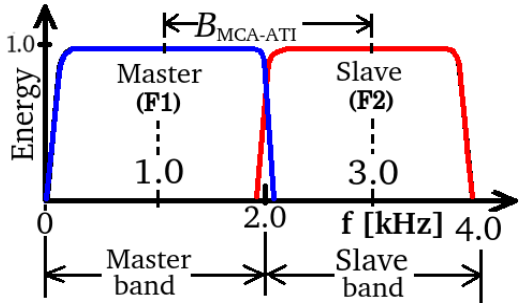

Fig. 2. Frequency allocation plan.

For completeness, we provide the expression of a signal returned by a point scatterer after the compression (matched filtering) for each non-overlapped sub-bands

$$r_i(t) = A\text{sinc}(\pi(t - 2R/c)) \cdot \exp\left\{ j\frac{4\pi R}{c/f_i} \right\}, \; i = 1, 2, \quad (4)$$

where A represents the amplitude of the received energy, t, R, and c are the time, the slant-range distance, and the velocity of the light, respectively, f_i represents the central frequency of each matched filter used to compress the signal. The adapted filter dynamically varies its bandwidth and central frequency to generate the two Doppler sub-apertures according to the frequency allocation scheme reported in Figure 2.

The entire procedure is summarized in Figure 3 which provides a block-scheme of the proposed processing chain which consists of 16 computational blocks, 3 fast Fourier transform (FFT), and 6 inverse-FFT. The input of the procedure is represented by full-polarimetric SAR raw data stored into stages number 1 (for the HH polarimetric channel), stage number 2 (for the HV polarimetric channel) and stage number 3 (for the VV polarimetric channel). The Doppler sub-apertures are generated for each polarimetric channel by the computational blocks number 4, 5, and 6, constituting the high-pass filters and by the computational blocks number 7, 8, and 9, which

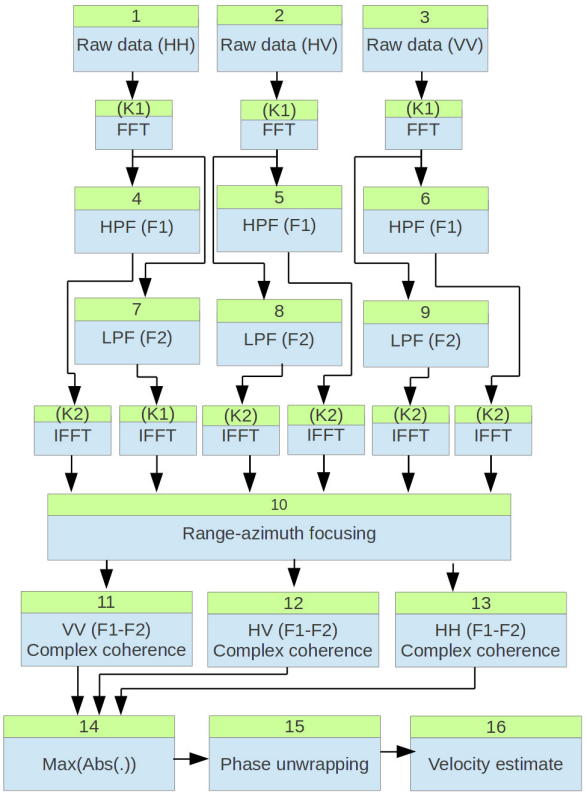

Fig. 3. Proposed Doppler velocity estimation procedure.

implement low-pass filters. All signals are transformed from the time domain into the frequency domain and vice-versa by computational blocks K1 and K2 respectively. All raw sub-apertures are focused by computational block 10, where a two-dimensional convolution between the raw data and the range-azimuth reference function is performed. Blocks number 11, 12, and 13 are devoted to the infra-chromatic complex coherence estimation according to the following procedure:

$$\tilde{\gamma}_{(n,m)} = \frac{E_{(n,m)}\left[r_1 r_2^{\dagger}\right]}{\sqrt{E_{(n,m)}\left[|r_1|^2\right] \cdot E_{(n,m)}\left[|r_2|^2\right]}}. \quad (5)$$

In (5) the complex coherence $\tilde{\gamma}$ is evaluated pixel by pixel processing two infra-chromatic SAR images r_1 and r_2 estimated from (4). The operator $E_{(n,m)}[\cdot]$ stands for the statistical expectation which in practice is approximated by the sampled average of a two-dimensional sliding investigation windows of size $n \times m$. The coherence in magnitude takes on values between 0 and 1 and provides an indication on the reliability level of the estimated interferometric phase coherence, which, according to (1), is proportional to the velocity of the rivers. Computational block 14 extracts pixel by pixel, the maximum of the coherency magnitude between all polarimetric channels with the objective to select the best reliable data. Computational block 15 performs the phase unwrapping based upon the algorithm proposed in [32], whereas computational block 16 estimates the river speed using coefficients that have been previously computed through a calibration process relying on the processing of a small database formed by ground stations.

The synthesized along-track virtual baseline can be computed according to (3) as

$$B_{MCA-ATI} = \frac{2v}{\Delta f_D}, \tag{6}$$

where Δf_D represents the Doppler shift between the two Doppler sub-apertures. An alternative expression for $B_{MCA-ATI}$ can be obtained from (1) as follows

$$\Delta\phi_{MCA-ATI} = \frac{4\pi u}{\lambda v} B_{MCA-ATI}, \tag{7}$$

where $\Delta\phi_{MCA-ATI}$ is the phase difference between the Doppler sub-apertures. Thus, exploiting (2), we obtain

$$B_{MCA-ATI} = \frac{\phi_D L v}{4\pi u} \Delta\phi_{MCA-ATI}, \tag{8}$$

where we have related the physical antenna size to the virtual baseline.

III. Experimental Results

In this section, illustrative examples are reported and commented. Specifically, in the next subsection, a spectral analysis of UAVSAR data is presented[1]. Precisely, the analysis is aimed at showing that UAVSAR data spectrum is suitable for MCA-ATI. To this end, we compare this spectrum with that of a white noise subject to the same processing as UAVSAR data and compute the critical ATI baseline, beyond which it is no longer allowed to assess single image ATI interferograms. Next, in Subsection III-B, the estimation results evaluated over real data are presented and discussed. In detail, in the first part of this subsection, a qualitative analysis is conducted due to the lack of ground-truth. Nevertheless, as shown by the estimated speed maps, the processing chain returns reasonable results since it is possible to appreciate speed variations towards low or high values where such variations are expected due to the river morphology. In the second part, the estimates returned by the proposed processing are validated by means of a comparison with data recorded by a ground station. As for real data, they are collected by a UAVSAR that transmits electromagnetic bursts centered at 1.26 GHz and with 80 MHz of chirp bandwidth allowing 3.5 m of range resolution. The swath in range is approximately 16 km, whereas the bandwidth along the azimuth direction is about 5 kHz with a resolution of 5 m. The useful parameters of the UAVSAR sensor are summarized in Tab. I [13]. Figure 2 represents the frequency allocation plan where the blue sub-apertures (each for the different polarizations), with label "Master-F1", are generated by computational blocks number 7, 8, and 9, and centered at 1.0 kHz, starting from 0 kHz up to 2.0 kHz. The red sub-apertures with label "Slave-F2" are generated by computational blocks number 4, 5 and 6, and centered at 3.0 kHz and starting from 2.0 kHz to 4.0 kHz. Both sub-apertures have less resolution with respect to the original full-band SAR image, this reduction amounts to approximately the 50% of the total Doppler Band. According to the spectrum allocation plan depicted in Figure 2, the frequency baseline is equal to 2 kHz. Now, observe that since the nominal platform velocity is equal to 243 m/s, the physical synthesized baseline is equal to $B_{MCA-ATI} = 0.24$ m which has a length sufficient for the objectives of this paper.

[1]UAVSAR data are freely available at https://uavsar.jpl.nasa.gov

TABLE I
UAVSAR Additional Details

Number	Item	Characteristic
1	Chirp bandwidth	80 MHz
2	PRF	4 kHz
3	PRT	0.23 ms
4	Antenna length	1.6 m
5	Type of acquisition	Stripmap
6	Polarization	Full-pol
7	Acquisition duration	22 s
8	Platform velocity	243 m/s
9	Observation height	5000 m

Two remarks are now in order. First, considering the "stripmap" acquisition of the UAVSAR sensor, we have split raw data in the frequency domain. This approach brings back the synthesis of a physical baseline referable to the equation (6) [14], [20], [21]. Second, it is important to notice that the total decorrelation is mainly due to three contributions, which can be classified as thermal, spatial and temporal [1]-[22, p. 307]. The thermal decorrelation is related to the Signal to Noise Ratio (SNR) of the radar signal, and, in most cases, the SNR is high enough to ignore this effect [23]. The spatial decorrelation is caused by the non zero ATI component of the baseline between the master and the slave images. In the present paper, the physical synthesized baseline is equal to $B_{MCA-ATI} = 0.24$ m and leads to a negligible factor [23]. Moreover, the two sub-apertures we synthesized are subjected to a sub-pixel and very fine co-registration in order to maximize the coherence. In the next section, we will show that the critical baseline beyond which the spatial decorrelation prevent us from using interferometry is much greater than $B_{MCA-ATI}$. Finally, the temporal decorrelation, which is caused by surface changes between the different temporal SAR acquisitions. Water surface could be a great source of decorrelation, but, it is important to stress here that coherence is computed by processing two Doppler sub-apertures synthesized by filtering a single SAR image.

A. Spectrum Analysis

In this subsection, an analysis in the frequency domain is presented in order to justify the application of the proposed method to the UAVSAR data. To this end, we compare the magnitude spectrum of the latter with that of a simulated white Gaussian process with $\mu = 0$ and $\sigma^2 = 1$ which undergoes the same processing chain as UAVSAR raw data. This comparison provides visual evidence of both the difference between such spectra and of the shape of the UAVSAR data spectrum. More importantly, we compute the critical ATI baseline, beyond which it is no longer allowed to assess single image ATI interferograms.

Figures 4 and 5 contain the magnitude spectrum of one range line (red line) and one azimuth line (red line) extracted

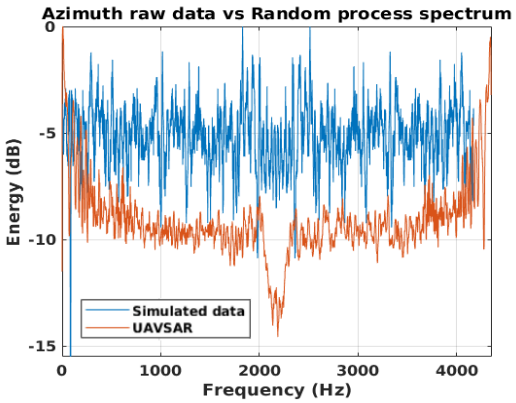

Fig. 4. Magnitude spectrum along azimuth for a given range.

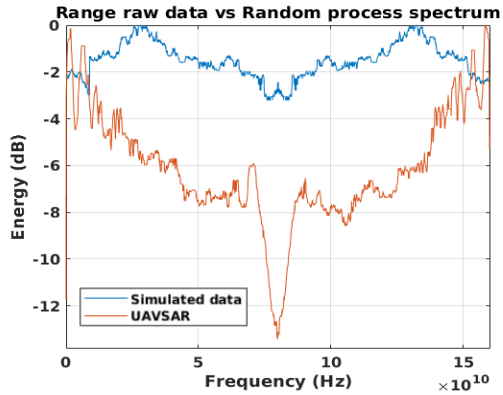

Fig. 5. Magnitude spectrum along range for a given azimuth.

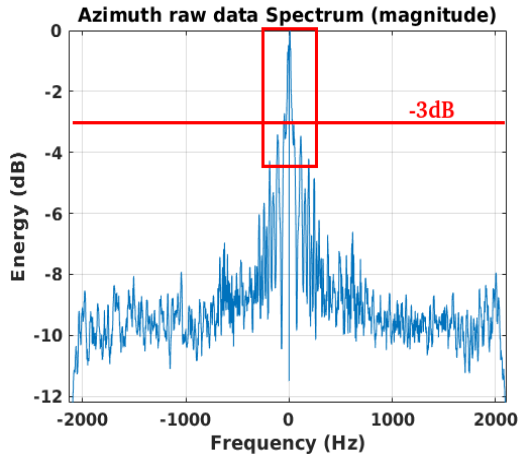

Fig. 6. UAVSAR raw data spectrum azimuth reflectivity profile (magnitude).

from UAVSAR raw data, respectively. The blue lines reported in these figures represent the magnitude spectrum of the simulated white random process. Moreover, in order to better appreciate its white nature, the simulated spectrum is filtered through a moving average filter using a 50×50 moving window. Inspection of the figures underlines that the data are well-sampled along both range and azimuth direction. As a matter of fact, the UAVSAR data spectrum is not flat but has a localized convexity in its central part with most of

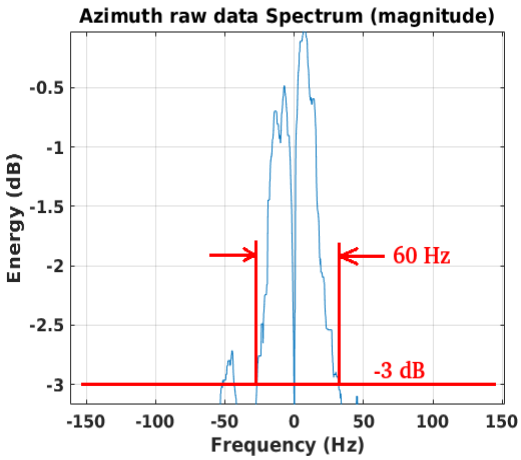

Fig. 7. 3 dB particular of the UAVSAR raw data spectrum azimuth reflectivity profile (magnitude).

the energy accumulated on the edges. Otherwise stated, it is possible to suitably appreciate the shape of the spectrum which is representative of a well-sampled signal and therefore very rich in information.

The critical baseline is computed by inverting a rough estimate of the UAVSAR bandwidth. In fact, the inverse of the bandwidth approximates data decorrelation time and, hence, given the platform velocity, it is possible to compute the distance at which ATI no longer makes sense. In Figure 6 we plot the spectrum of the UAVSAR raw data centered at the zero frequency (fftshift() function provided by Matlab has been used), while in Figure 7 we magnify the detail contained within the red box shown in Figure 6. The figure points out that the 3 dB bandwidth is equal to about 60 Hz. Now, exploiting (6), the critical baseline exhibits a value of about 8 meters which is much greater than the virtual baseline (0.24 m) synthesized by the proposed method. Summarizing, the application of MCA preserves a level of correlation that allows for ATI at least for the considered parameter setting.

B. Experimental results on Real Datasets

As stated before, this subsection is split into two parts. The first part reports a qualitative analysis (due to the lack of the ground-truth) over two different datasets, which allows appreciating speed variations at those locations where they are expected according to the river path. The second part contains a quantitative analysis conducted resorting to speed measurements recorded by a ground station. Finally, the velocity maps shown in the following are obtained by applying a mask that removes the speed components of the vegetation, which are not of interest.

1) Qualitative Analysis on two datasets: The first study case exploit data contained in ColFor_30402_14039_010_140414_L090_CX_01_mlc. The resulting SAR image is shown in Figure 8 where the point $P1$ represents the image center which is geolocated at the following coordinates: 1.580775°N 78.618778°W. The image is orthorectified and displayed using the Pauli color-scale where

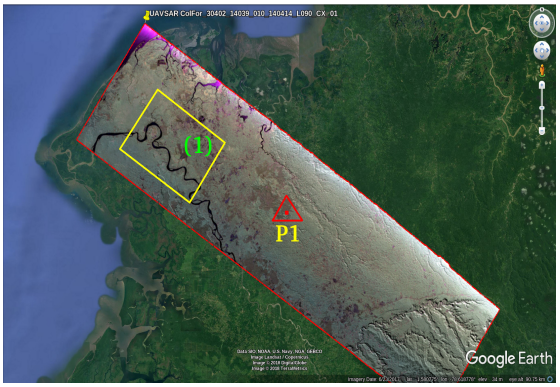

Fig. 8. Case of study number one orthorectified SAR image in the Pauli base.

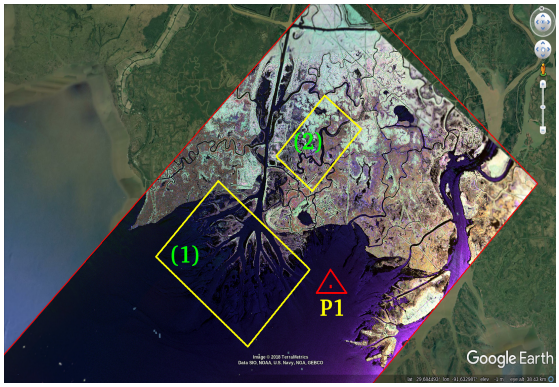

Fig. 9. Case of study number two orthorectified SAR image in the Pauli base.

- the red color is assigned to the double-bounce scattering events raising from the composed polarimetric signal obtained as[2] $s11 - s22$;
- the green color, representing the volume scattering, is associated to the signal $2 \cdot s12$;
- the blue channel, the single-bounce scattering events, is assigned to the polarimetric signal obtained by combining $s11$ and $s22$ as $s11 + s22$.

The ROI is located inside the yellow box labeled with 1 in Figure 8. The second study case relies on data with identification number: gulfco_05003_15057_007_150508_L090_CX_01_mlc. The corresponding Pauli-based orthorectified SAR image is shown in Figure 9 where the point $P1$ represents the image center geolocated at 29.477644°N 91.378587°W. In this case, two ROIs are considered and are indicated in the figure by means of the yellow boxes tagged by 1 and 2.

Figure 10 contains the velocity map for study case number one, where the river is correctly detected with an infra-chromatic coherence greater than 0.88. Specifically, each pixel of the image represents the Doppler velocity estimate returned by computational block 15 (see Figure 3). The target is the river Rio Mataje located in the state of Colombia and the maximum value of the estimated water-flow velocity is about 1.4 m/s. The figure also highlights that the estimated velocity in the segments that are almost parallel to the azimuth direction is very low whereas the river segments containing a component along the range direction exhibit nonzero velocities that become large when the river aligned with the range direction. In Figure 11, the area within the yellow box number one of Figure 10 is magnified to highlight the presence of a bottleneck where, as expected, an increase of velocity occurs. This situation confirms that the proposed technique can identify the changes in the river Doppler velocity.

Figure 12 refers to the study case number two, where the Atchafalaya river is correctly detected with an infra-chromatic coherence greater than 0.80. This river is a distributary of Mississippi river and has a length of about 137 miles (220 km). Moreover, it is the fifth largest river in North America. The figure shows the velocity estimated for each point belonging to the yellow box number one of Figure 9. Specifically, the

[2]Note that $s11$, $s12$, and $s22$ are the polarimetric channels.

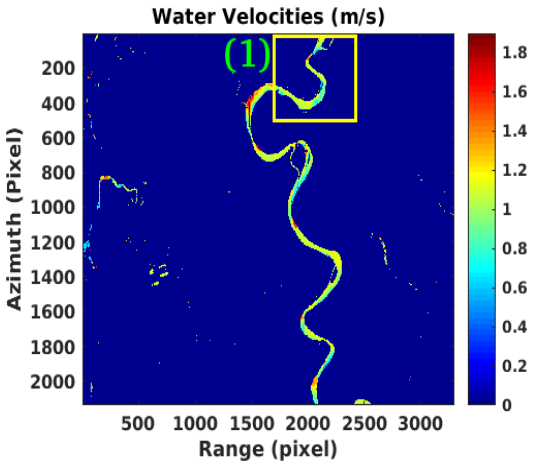

Fig. 10. Case of study one river Doppler velocity map.

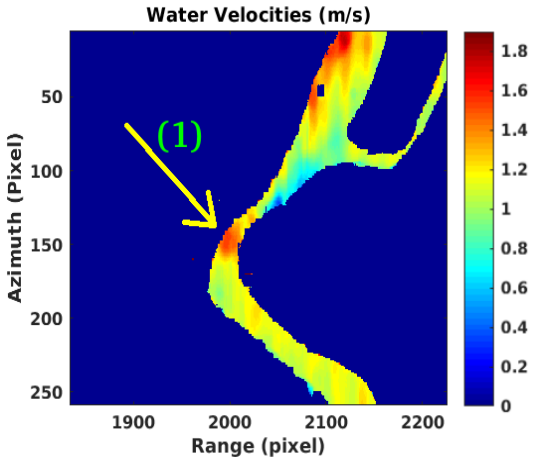

Fig. 11. Particular of the case of study one river Doppler velocity map.

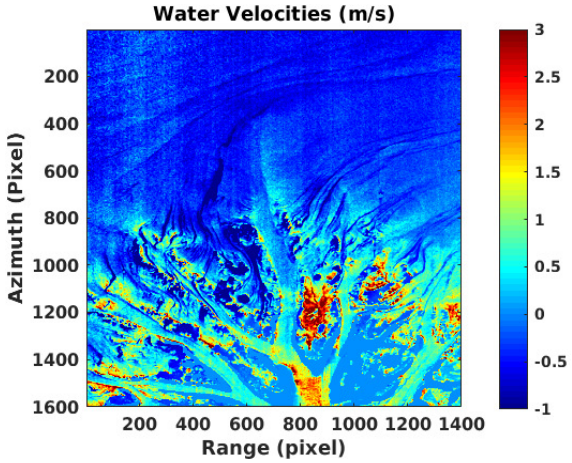

Fig. 12. Case of study two river Doppler velocity map.

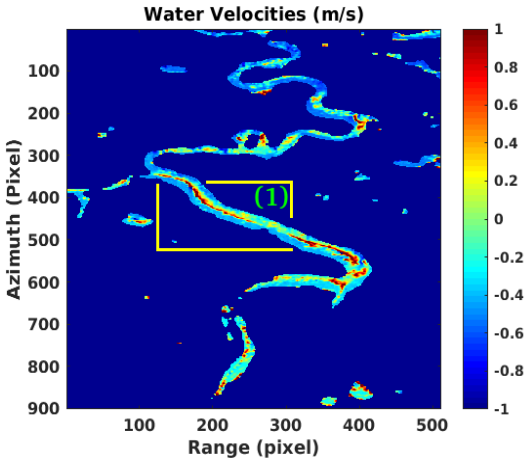

Fig. 13. Case of study two river Doppler velocity map.

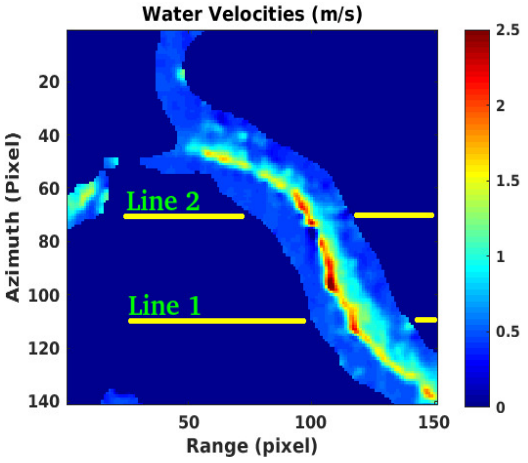

Fig. 14. Particular of the case of study two river Doppler velocity map.

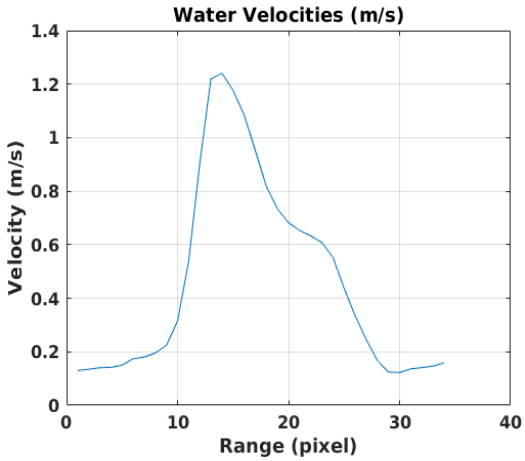

Fig. 15. Line one river Doppler velocity profile for the second study case.

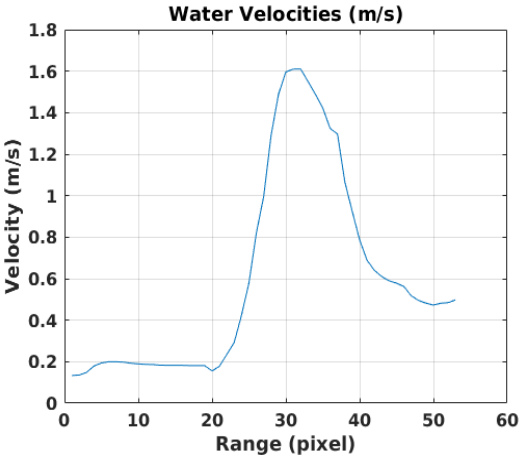

Fig. 16. Line two river Doppler velocity profile for the second study case.

great mouth of the river can be observed along with the spatial evolution of the Doppler velocities of the river that are recomposed with those of the sea. The region contained in the yellow box labeled with 2 in Figure 9 is analyzed in Figure 13. The velocities of the river are compliant with the physical principle that higher velocities are present at the river center and lower velocities are detected along the river edges. This phenomenon is due to the fact that the edges generate more friction lowering the velocity of the water flow, which increases as the center is approaching. In Figure 14, the region contained in the yellow box of Figure 13 is suitably magnified. The figure shows detailed information about the river water-flow velocity. Finally, in Figure 15 and Figure 16, the behavior of the instantaneous velocity of the river versus range is plotted using data belonging to the two lines shown in Figure 14. The curve shapes reflect the physical evolution of the water-flow.

2) Quantitative Analysis: In this last study case, a portion of the US state of Alaska collected by the UAVSAR is considered. The resulting Pauli-based orthorectified SAR image is shown in Figure 17. Moreover, the validation of the measurements is performed comparing the water-flow velocity estimates with data observed by the water-level measurement station having the following identification number: *USGS*

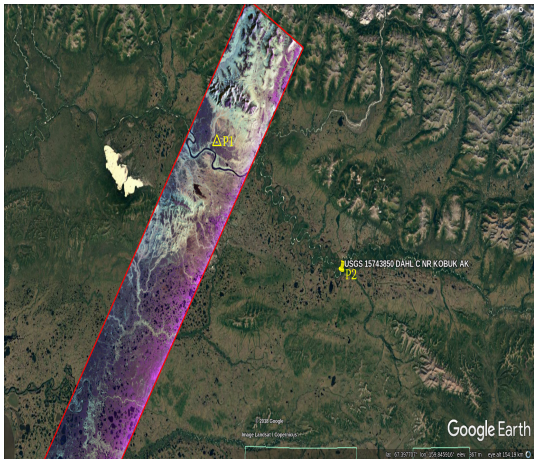

Fig. 17. Case of study number three orthorectified SAR image in the Pauli base.

15743850 DAHL C NR KOBUK AK. Data are made freely available by the United-States National Water Information System web interface. Point $P1$ is geolocated at the following coordinates: Datum world geodetic system 1984 (WGS 84) European petroleum survey group (EPSG) 4230, Lat: 67.119946° N, Lon: 158.177811° W; while point $P2$ (the measurement station) is instead geolocated at the following coordinates: Datum WGS 84 EPSG 4230, Lat: 66.848357° N, Lon: 157.190757° W. Only one pair of along-track full-polarimetric SAR images is synthesized by dividing the total range-Doppler history into two groups (a master and a slave ATI SAR images couple) according to the frequency allocation plan reported in Figure 2. This method leads to Moving Target Indicator SAR channels with relatively high Signal to Noise Ratio values. Additionally, in order to improve the MTI performance in term of sensitivity, the synthetic baseline is maximized according to a strategy that partitions the Doppler band to minimize the overlapped region. Thus, according to [24], the resulting physical ATI baseline is approximately 0.5 m. The measurement station (point $P2$) is distant approximately 30 km from $P1$, therefore a small error on the experimental results comparison is possible and acceptable. The list of SAR data identification codes (ICs) and acquisition date are reported in Tab. II. The processed time series of SAR data is that spatially and temporally closest to the measurement station. Figure 18 represents the velocity map estimated on the first UAVSAR data reported in Tab. II. The red box located in the figure contains the area that has been investigated in detail in Figures 19. For all the datasets, the velocity measurements used for validation purposes refers to that picture. The infra-chromatic coherency in magnitude and phase are reported in Figure 20 and Figure 21 respectively. It can be observed that the river is detected with very high coherence and, consequently, the phase is highly stable.

Due to the difficulty in finding ground truths concerning the speeds of the water masses of rivers, the obtained velocity estimates are compared with the heights of the water level measured by the ground station. As a matter of fact, there exists a correlation between the height and the velocity of a river

TABLE II
UAVSAR DATA FULL-POLARIMETRIC ADDITIONAL DETAILS

Number	Product Identification	Date
1	permaf03108151470041510O5L090	05-10-2015
2	ambler030011709700817O915L090	15-09-2017
3	PREMLEG0300117067006170619	19-06-2017
4	ambler030011805400918O901L090	01-09-2018

TABLE III
OBTAINED ESTIMATES VERSUS STATION MEASUREMENTS

Number	Water Height (m)	Discharge (cubic-feet/s)	SAR velocity (m/s)
1	4.9	35	0,74
2	5.7	280	1,17
3	4.75	20	0,63
4	4.75	35	0,71

water mass [26]- [28]. The validation procedure implemented is the following: the first SAR image of Tab. II was used to calibrate the system as reported in [30], taking into account the physical dimensions of the watercourse; the calibration coefficients are used to obtain the velocity estimates for the other datasets.

Figure 22 represents the height of the water-flow observed by the measurement station, which is reporting the daily water height starting from the 01-09-2015 to 31-10-2015. The UAVSAR observation was performed on the 05-10-2015 which is indicated on the time span by a red arrow. The measurement on that day is approximately 4.9 feet. Figure 23 shows the discharge in cubic feet per seconds recorded during the same time-span of the previous picture. Figure 22 and Figure 23 are synchronized to the UAVSAR observation ID: permaf03108151470041510O5L090, Figure 24 and Figure 25 are synchronized to the UAVSAR observation ID: ambler030011709700817O915L090, Figure 26 and Figure 27 are synchronized to the UAVSAR observation ID: PREMLEG0300117067006170619, Figure 28 and Figure 29 are synchronized to the UAVSAR observation ID: ambler030011805400918O901L090. The results observed by the UAVSAR are compared to the observations recorded by the measurements station are reported in Tab. III. The precision of the SAR measurements are confirmed by an increasing of velocity correctly detected on the records number 2 reported in Tab. II and Tab. III.

As concluding remark of this section, it is worth noticing that the main limitation of this technique is represented by the azimuth resolution degradation of ATI interferograms. As a matter of fact, Doppler band used for each sub-aperture is lower than the entire Doppler band and, hence, the resolution decreases. Moreover, in order to obtain a good spectral representation of data high sampling rates are required with the consequence that high performance electronic components are required and the amount of data can precociously saturate the

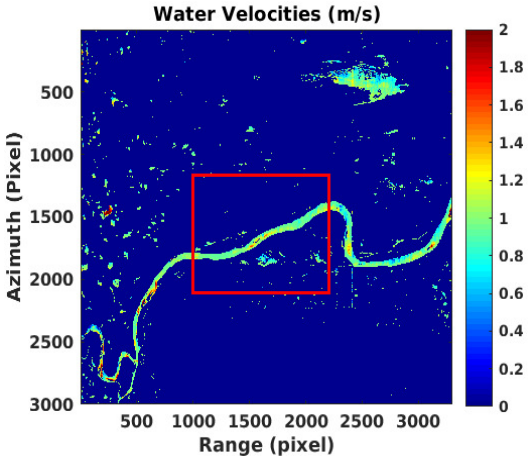

Fig. 18. Case of study three river Doppler velocity map.

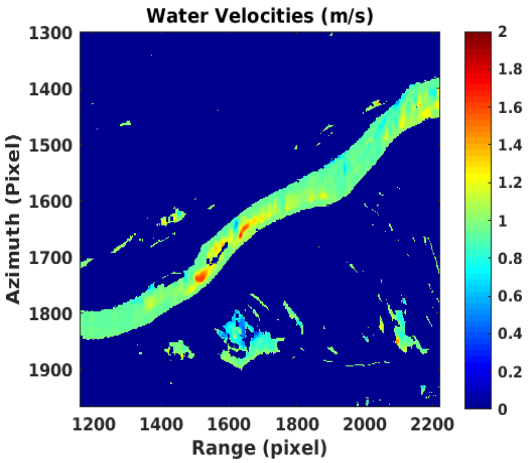

Fig. 19. Particular of the case of study three river Doppler velocity map.

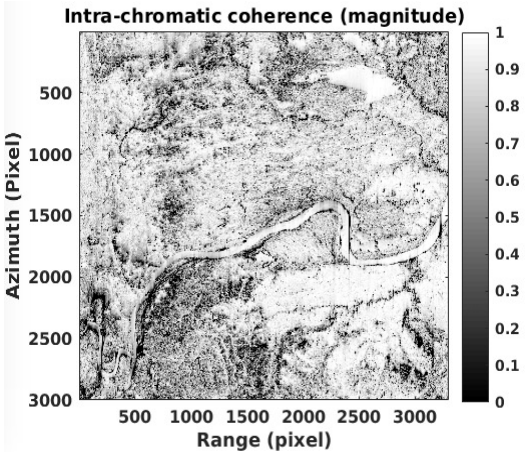

Fig. 20. Infra-chromatic coherence (magnitude).

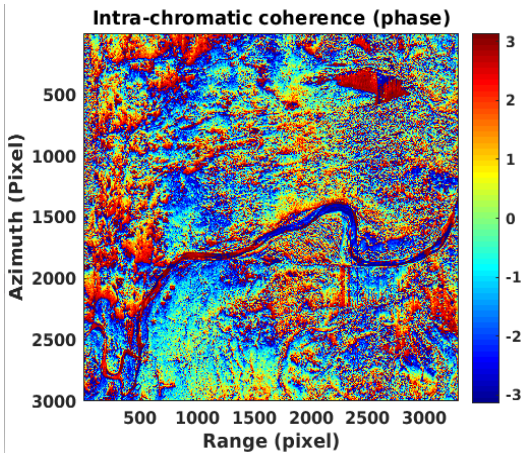

Fig. 21. Infra-chromatic coherence (phase).

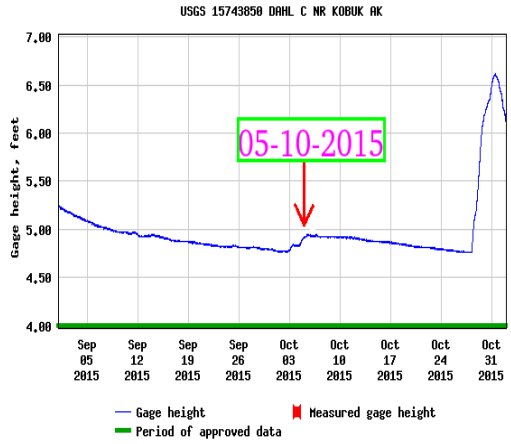

Fig. 22. Terrain measurements station observations (water height).

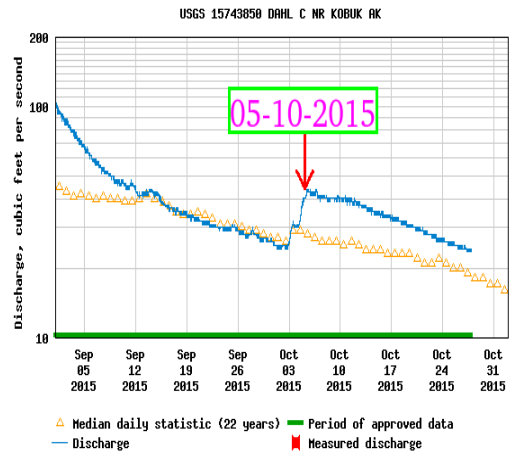

Fig. 23. Terrain measurements station observations (water discharge).

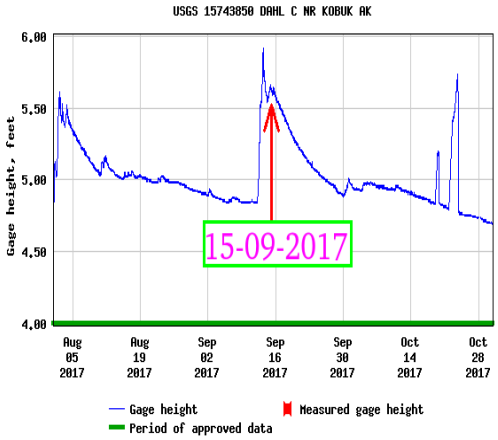

Fig. 24. Terrain measurements station observations (water height).

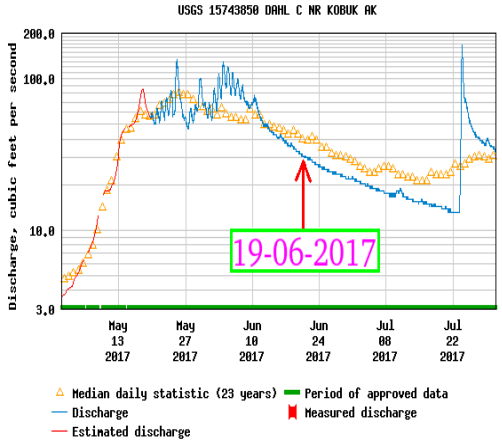

Fig. 27. Terrain measurements station observations (water discharge).

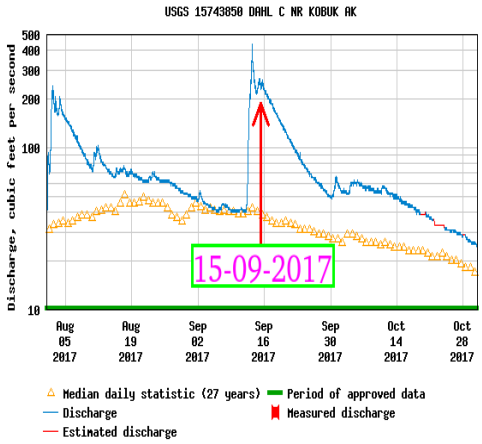

Fig. 25. Terrain measurements station observations (water discharge).

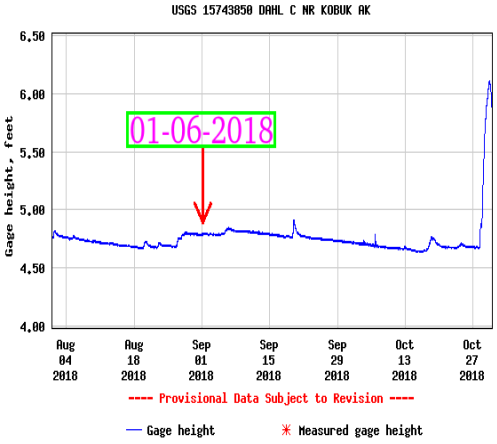

Fig. 28. Terrain measurements station observations (water heights).

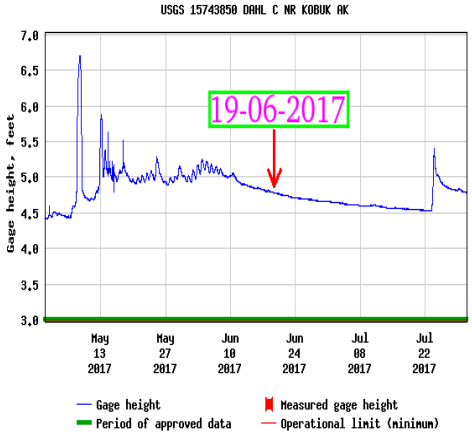

Fig. 26. Terrain measurements station observations (water hights).

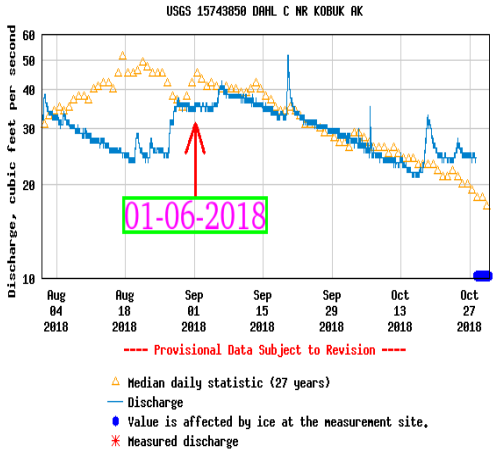

Fig. 29. Terrain measurements station observations (water discharge).

on-board sensor memory. As for the azimuth direction, data oversampling is achieved by increasing the pulse repetition frequency (PRF). In SAR systems, the higher the PRF, the lower the swath in range.

IV. Conclusions

In this paper, a novel SAR processing scheme aimed at performing ATI using only one airborne flight track to estimate river flow velocities is designed and assessed. Specifically, the MCA has been applied in the Doppler domain and combined with along-track SAR interferometry defining a new approach called MCA-ATI-SAR technique. This kind of processing can be exploited as an effective means to measure the water surface speed for rivers, since it can be estimated using data from a single-pass acquisition, allowing the construction of a worldwide database containing historical and reliable data, which nowadays is missing. As a matter of fact, the performance analysis, conducted on several real recorded UAVSAR datasets, has highlighted the capability of MCA-ATI-SAR technique to track water flow speed variations along the river itinerary. Specifically, the experimental results have pointed out that such techniques returns high speed values at the locations where such values are expected due to the river morphology. Besides, at least for the considered datasets, the obtained estimates are coherent with the height measurements provided by a ground station corroborating the effectiveness of the MCA-ATI-SAR technique.

References

[1] R. M. Goldstein, H. A. Zebker, "Interferometric radar measurement of ocean surface currents," *Nature*, Vol. 328, no. 6132, pp. 707, 1987.

[2] R. Romeiser et al., "Current measurements by SAR along-track interferometry from a Space Shuttle," *IEEE Transactions on Geoscience and Remote Sensing*, vol. 43, no. 10, pp. 2315-2324, Oct. 2005.

[3] J. F. Nouvel, P. Dubois-Fernandez, P. Kosuth and Y. Lasne, "Along Track Interferometry on Rhone River," *IGARSS 2008 - 2008 IEEE International Geoscience and Remote Sensing Symposium*, Boston, MA, pp. Vol. 495-V, no. 497, 2008.

[4] Duk-jin Kim, W. M. Moon, D. Moller and D. A. Imel, "Measurements of ocean surface waves and currents using L- and C-band along-track interferometric SAR," *IEEE Transactions on Geoscience and Remote Sensing*, vol. 41, no. 12, pp. 2821-2832, Dec. 2003.

[5] F. Lombardini, F. Bordoni, F. Gini and L. Verrazzani, "Multibaseline ATI-SAR for robust ocean surface velocity estimation," *IEEE Trans. on Aerosp. and Electr. Systems*, vol. 40, no. 2, pp. 417-433, Apr. 2004.

[6] M. A. Sletten, "An analysis of gradient-induced distortion in ATI-SAR imagery of surface currents," *IEEE Transactions on Geoscience and Remote Sensing*, vol. 44, no. 7, pp. 1995-2002, July 2006.

[7] S. J. Frasier and A. J. Camps, "Dual-beam interferometry for ocean surface current vector mapping," *IEEE Transactions on Geoscience and Remote Sensing*, vol. 39, no. 2, pp. 401-414, Feb 2001.

[8] R. Siegmund, Mingquan Bao, S. Lehner and R. Mayerle, "First demonstration of surface currents imaged by hybrid along- and cross-track interferometric SAR," *IEEE Transactions on Geoscience and Remote Sensing*, vol. 42, no. 3, pp. 511-519, March 2004.

[9] F. Biondi, "Low rank plus sparse decomposition of synthetic aperture radar data for maritime surveillance," *2016 4th International Workshop on Compressed Sensing Theory and its Applications to Radar, Sonar and Remote Sensing (CoSeRa)*, Aachen, 2016, pp. 75-79.

[10] F. Biondi, "Low-Rank Plus Sparse Decomposition and Localized Radon Transform for Ship-Wake Detection in Synthetic Aperture Radar Images," *in IEEE Geoscience and Remote Sensing Letters*, vol. 15, no. 1, pp. 117-121, Jan. 2018.

[11] F. Biondi, "(L + S)-RT-CCD for Terrain Paths Monitoring," in *IEEE Geoscience and Remote Sensing Letters*, vol. 15, no. 8, pp. 1209-1213, Aug. 2018.

[12] F. Mètivier, "Diffusive-like buffering and saturation of large rivers," *Physical Review*, vol. 60, no. 5, pp. 5827, 1999.

[13] P. A. Rosen, S. Hensley, K. Wheeler, G. Sadowy, T. Miller, S. Shaffer, S. Madsen, "UAVSAR: a new NASA airborne SAR system for science and technology research," *2006 IEEE Conference on Radar*, Verona, NY, USA, pp. 8-, 2006.

[14] F. Biondi, "COSMO-SkyMed Staring Spotlight SAR Data for Micro-Motion and Inclination Angle Estimation of Ships by Pixel Tracking and Convex Optimization," *Rem. Sens.*, Vol. 11, no. 7, pp. 766, 2019.

[15] F. Biondi, P. Addabbo, D. Orlando, and C. Clemente, "Micro-Motion Estimation of Maritime Targets Using Pixel Tracking in Cosmo-Skymed Synthetic Aperture Radar Data - An Operative Assessment," *Remote Sensing*, Vol. 11, no. 14, pp. 1637, 2019.

[16] F. Biondi, A. Tarpanelli, P. Addabbo, C. Clemente. and D. Orlando, "Pixel Tracking to Estimate Rivers Water Flow Elevation Using Cosmo-SkyMed Synthetic Aperture Radar Data" *Remote Sensing*, Vol. 11, no. 21, pp. 2574, 2019.

[17] S. L. Ullo, P. Addabbo, D. Di Martire, S. Sica, N. Fiscante, L. Cicala, C. V. Angelino, "Application of DInSAR Technique to High Coherence Sentinel-1 Images for Dam Monitoring and Result Validation Through In Situ Measurements", *IEEE Journal of Selected Topics in Applied Earth Observations and Remote Sensing*, vol. 12, no. 3, pp. 875-890, March 2019.

[18] P. Addabbo, F. Biondi, C. Clemente, D. Orlando and L. Pallotta, "Classification of Covariance Matrix Eigenvalues in Polarimetric SAR for Environmental Monitoring Applications," *IEEE Aerospace and Electronic Systems Magazine*, vol. 34, no. 6, pp. 28-43, 1 June 2019.

[19] F. Biondi, C. Clemente and D. Orlando, "An Eigenvalue-Based Approach for Structure Classification in Polarimetric SAR Images", *IEEE Geoscience and Remote Sensing Letters*.

[20] C. V. Jakowatz, D. E. Wahl, P. H. Eichel, D. C. Ghiglia, P. A. Thompson, "Spotlight-Mode Synthetic Aperture Radar: A Signal Processing Approach: A Signal Processing Approach," *Springer Science & Business Media*, 2012.

[21] N. Veneziani, F. Bovenga, and A. Refice, "A wide-band approach to the absolute phase retrieval in SAR interferometry," *Radar Signal Processing and Its Applic.*, Springer, Boston, MA, pp. 183-205, 2003.

[22] J. S. Lee, E. Pottier, "Polarimetric radar imaging: from basics to applications," *CRC press*, 2009.

[23] H. A. Zebker and J. Villasenor, "Decorrelation in interferometric radar echoes," *in IEEE Transactions on Geoscience and Remote Sensing*, vol. 30, no. 5, pp. 950-959, Sept. 1992.

[24] J. M. B. Dias and P. A. C. Marques, "Multiple moving target detection and trajectory estimation using a single SAR sensor," *IEEE Transactions on Aerospace and Electronic Systems*, vol. 39, no. 2, pp. 604-624, April 2003.

[25] F. Lombardini, F. Bordoni and F. Gini, "Feasibility study of along-track SAR interferometry with the COSMO-Skymed satellite system," *IGARSS 2004. 2004 IEEE International Geoscience and Remote Sensing Symposium, Anchorage, AK*, vol.5, pp. 3337-3340, 2004.

[26] G. R. Brakenridge, et al. "Calibration of satellite measurements of river discharge using a global hydrology model," *Journal of hydrology*, Vol. 475, pp. 123-136, 2012.

[27] S. Calmant, and F. Seyler, "Continental surface waters from satellite altimetry," *Comptes Rendus Geoscience*, Vol 338, no. 14-15, pp.1113-1122, 2006.

[28] A. Tarpanelli, et al., "River discharge estimation by using altimetry data and simplified flood routing modeling," *Remote Sensing*, Vol. 5, no.9, pp. 4145-4162, 2013.

[29] Yen, Ben Chie, "Open channel flow resistance," *Journal of hydraulic engineering*, Vol. 128, no. 1, pp. 20-39, 2002.

[30] D.M. Bjerklie, D. Moller, L. C. Smith, S. L. Dingman, "Estimating discharge in rivers using remotely sensed hydraulic information," *Journal of hydrology*, Vol. 309, no. 1-4, pp. 191-209, 2005.

[31] J. E. Costa, K. R. Spicer, R. T. Cheng, F. P. Haeni, N. B. Melcher, E. M. Thurman, W. C. Keller, "Measuring stream discharge by non-contact methods: A proof-of-concept experiment," *Geophysical Research Letters*, Vol. 27, no.4, pp. 553-556, 2000.

[32] R. M. Goldstein, H. A. Zebker, and C. L. Werner, "Satellite radar interferometry: Two-dimensional phase unwrapping," in *Radio Science*, vol. 23, no. 4, pp. 713-720, July-Aug. 1988.